Journal of Engineering Mathematics (2024) 144:14
https://doi.org/10.1007/s10665-023-10314-2

Numerical validation of analytical formulas for channel flows over liquid-infused surfaces

Hiroyuki Miyoshi[1] · **Henry Rodriguez-Broadbent**[1] · **Darren G. Crowdy**[1]

Received: 4 July 2023 / Accepted: 21 November 2023 / Published online: 17 January 2024

Abstract
This paper provides numerical validation of some new explicit, asymptotically exact, analytical formulas describing channel flows over liquid-infused surfaces, an important class of surfaces of current interest in surface engineering. The new asymptotic formulas, reproduced here, were derived in a recent companion paper by the authors. The numerical validation is done by presenting a novel computational method for calculating longitudinal flow in a periodic channel involving finite-length closed liquid-filled grooves with a flat two-fluid interface, a challenging problem given the two-fluid nature of the flow. The formulas are asymptotically exact for wide channels where the grooves on the lower wall of the channel are well separated; the numerical method devised here, however, is subject to no such restrictions. Significantly, it is shown here that the asymptotic formulas remain good global approximants for the flow over a wide range of flow geometries, including those well outside the asymptotic parameter range for which they were derived. It is found that the formulas are more reliable for liquid-infused surfaces than for superhydrophobic surfaces.

Keywords Asymptotics · Conformal maps · Generalized Schwarz integral formulae · Liquid-infused surfaces · Schwarz integral formulae

1 Introduction

In a recent paper [1] the authors used a three-stage asymptotic analysis to derive explicit analytical formulas describing, to leading order in the asymptotic approximations, the longitudinal channel flow over a liquid-infused surface (LIS). Such surfaces are the subject of much recent interest to the surface engineering community owing to their diverse uses in applications: a recent review [2] surveys many of these. In the scenario considered, the fluid is taken to flow along the direction of alignment of a series of

✉ Hiroyuki Miyoshi
hiroyuki.miyoshi17@imperial.ac.uk

[1] Department of Mathematics, Imperial College London, 180 Queen's Gate, London SW7 2AZ, UK

parallel grooves etched into the lower wall of a channel. The upper wall of the channel is taken to be a no-slip surface. The flow is driven along the channel by an imposed pressure gradient. The grooves in the lower wall are much longer than they are wide, and they can be open or closed. Closed grooves, which might also be referred to as "trenches", have upstream and downstream ends and the fluid in them experiences a reverse pressure gradient causing it to engage in a recirculating flow in the grooves [3]. Given the complexities of such a two-phase flow scenario, the possibility of finding any analytical formula describing it is unexpected. This renders the formula found in [1] of some theoretical significance and it is important to assess its usefulness. That is the purpose of this paper.

Figure 1 shows a typical two-fluid scenario as an (x^*, y^*) cross-section at a typical Z^* station in a Cartesian (x^*, y^*, Z^*) coordinate system where the flow of both fluids is assumed to be in the "axial", or streamwise, Z^* direction. The main outcome of Rodriguez-Broadbent *et al.* [1] is now summarized. They show that, away from the upstream and downstream ends of well-separated circular grooves protruding by angle θ_2 down into the lower channel wall, and where the interface protrudes by angle θ_1 into the upper fluid, the coupled leading order axial velocity fields in the two-fluid phases are given by the explicit formulas

$$\tilde{w}_1^*(x^*, y^*) = \frac{\partial p_1^*}{\partial Z^*}\frac{H^2}{\mu_1}\tilde{w}_1\left(\frac{x^*}{H}, \frac{y^*}{H}\right), \quad \tilde{w}_2^*(x^*, y^*) = \frac{\partial p_1^*}{\partial Z^*}\frac{H^2}{\mu_2}\tilde{w}_2\left(\frac{x^*}{H}, \frac{y^*}{H}\right), \tag{1}$$

with

$$\tilde{w}_1(x, y) \sim \frac{1}{2}y^2 + \frac{\delta\alpha}{2 + \Delta\delta^2\alpha\pi}\left(W_b\left(\frac{x}{\delta\alpha}, \frac{y}{\delta\alpha}\right) + \delta\alpha\Delta\frac{y}{x^2 + y^2} + \frac{\Delta\delta\pi}{2}\frac{\sinh(\pi y/\alpha)}{\cos(\pi x/\alpha) - \cosh(\pi y/\alpha)}\right), \tag{2}$$

$$\tilde{w}_2(x, y) \sim \frac{\delta\alpha}{2 + \Delta\delta^2\alpha\pi}W_g\left(\frac{x}{\delta\alpha}, \frac{y}{\delta\alpha}\right), \tag{3}$$

where $\alpha = L/H$, $\delta = a/L$, $\sigma = \mu_2/\mu_1$, and

$$W_b(x', y') = -y' + \frac{1}{2\pi}\mathrm{Im}\left[\fint_{-\infty}^{\infty}\rho_b(k)\left(\frac{1 + (x' + \mathrm{i}y')}{1 - (x' + \mathrm{i}y')}\right)^{\mathrm{i}k}\mathrm{d}k\right],$$
$$W_g(x', y') = \frac{\mathcal{S}}{4}(1 - x'^2 - y'^2) + \frac{1}{2\pi}\mathrm{Im}\left[\fint_{-\infty}^{\infty}\rho_g(k)\left(\frac{1 + (x' + \mathrm{i}y')}{1 - (x' + \mathrm{i}y')}\right)^{\mathrm{i}k}\mathrm{d}k\right], \tag{4}$$
$$\Delta = \frac{\mathrm{i}}{\pi}\fint_{-\infty}^{\infty}ke^{-k\pi}\rho_b(k)\mathrm{d}k.$$

Here $\fint$ denotes the principal part integral and explicit formulas for $\rho_b(k)$ and $\rho_g(k)$ are given in Appendix A. When a relevant capillary number is small [1] the interface protrusion angle θ_1 will vary only slowly in the streamwise direction, i.e. $\theta_1 = \theta_1(Z^*)$,

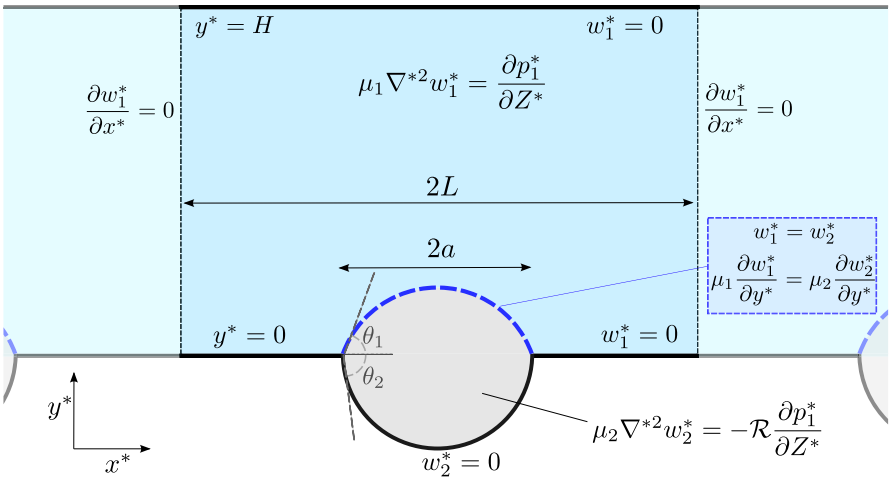

Fig. 1 Cross-section of the boundary value problem relevant for channel flow over a liquid-infused surface as considered in [1] under a "slender groove" assumption. The fluid interface protrudes into fluid 1 by angle θ_1 and the circular grooves protrude down into the solid substrate by angle θ_2.

and the formulas above give the leading order cross-plane flows at that Z^* location.

The formulas reported above are derived under the asymptotic assumptions that $\alpha = L/H \ll 1$ and $\delta = a/L \ll 1$. This means that the upper channel wall is not too close to the lower liquid-infused surface, and that the grooves etched on the lower wall are not too close together. The present paper carries out a numerical study to assess the scope and value of these formulas, the only restriction being that the interface is flat, i.e. $\theta_1 = 0$ (this requirement is necessitated by the nature of the numerical method devised here). All other geometrical features of the flow, such as α, δ, and θ_2 are, however, variable which means that the numerical method can test the accuracy of results given by the asymptotic formulas as these parameters are varied. Remarkably, it is found here that the formulas provide excellent approximations for the flows over liquid-infused surfaces even well outside their expected range of validity, that is, when α and δ are not necessarily small. While this is only tested here for $\theta_1 = 0$ we conjecture it remains true for other values of θ_1 that are sufficiently small.

While many previous authors have studied similar problems using a range of methods, the authors are not aware of any previous analytical results that have been derived without making heuristic assumptions. Such assumptions are often made to simplify the challenging coupled two-fluid problem. Schönecker *et al.* [4, 5] make the assumption that the interfacial shear stress is constant and offer strategies for approximating this constant value. Nizkaya *et al.* [6] use a so-called gas cushion model to study unbounded flow over periodic arrays of fluid-filled grooves with flat interfaces. Crowdy [7] studied rectangular fluid-filled grooves, with flat and weakly curved interfaces, using perturbation methods relevant for small and large viscosity contrasts but without making any heuristic assumptions.

There are many numerical studies of this two-fluid scenario. Ng *et al.* [8] used Fourier series in a numerical study of channel flow over closed grooves filled with a second fluid. They study both longitudinal and transverse flow scenarios for arbitrary viscosity contrast but only for flat interfaces. Moreover for the longitudinal flow they do not incorporate any longitudinal (axial) variation. Ge *et al*. [9] used finite element methods to resolve transverse flows over LISs incorporating interface curvature and the situation where the interface invades the grooves. Their interest is in studying the phenomenon of shear-induced failure whereby the subphase fluid can be dragged out of the grooves. Liu *et al.* [10] have investigated shear-driven failure for longitudinal channel flows over liquid-infused surfaces by making certain heuristic assumptions regarding the interface conditions. They consider the longitudinal evolution of the two-phase interface in order to characterize the failure mechanism and build on an earlier theoretical study by Wexler *et al.* [3]. Game *et al.* [11] used domain decomposition techniques to study longitudinal flow along unidirectional surfaces where the dynamical effects of a subphase fluid are also resolved but where they assume there is no axial variation of the geometry. Later, Game *et al.* [12] carried out an asymptotic expansion relevant at small capillary numbers to describe the slow axial evolution of the protrusion angle of the menisci in a model of longitudinal flow over a superhydrophobic surface but now ignoring the effects of the subphase fluid; the formulas in [1] extend this approach to the case of two fluids interacting across an interface. Ji *et al.* [13] use dual series and reciprocity relations to solve for two-phase flow with flat interfaces with a focus on quantifying the slip properties of these surfaces.

In this paper, the aim is to validate the analytical result given by [1] by presenting a new method for calculating longitudinal flows in a periodic channel involving closed liquid-filled grooves whose interfaces are flat. The method uses tools already employed in a study of superhydrophobic surfaces [14] but several features are different. In particular, while use is made of a conformal mapping from a triply connected preimage region described in Miyoshi *et al.* [14], the problems considered here involve two fluids, and their coupling across an interface is required. This is achieved here by making use of new mathematical tools known as "generalized Schwarz integrals" as constructed recently by Miyoshi and Crowdy [15]. A second conformal mapping from a simply connected disc to the groove region is also used to weld the flows together at the interface.

The structure of this paper is as follows. Section 2 explains the problem formulation and defines boundary value problem associated with the two-fluid setting. Section 3 introduces a complex analysis formulation and the relevant conformal mappings on which the method is based. The main findings are presented in Sect. 4 which gives numerical comparisons with the analytical predictions of formulas (2). Although it is not the primary aim of this work, Sect. 5 shows numerical results for velocity profiles on the interface and calculates useful quantities such as the effective slip lengths associated with the flows. Section 6 explains how the method is easily adaptable to account for other groove shapes and includes some illustrative calculations for triangular and rectangular grooves. Finally, Sect. 7 discusses the results and describes the future work.

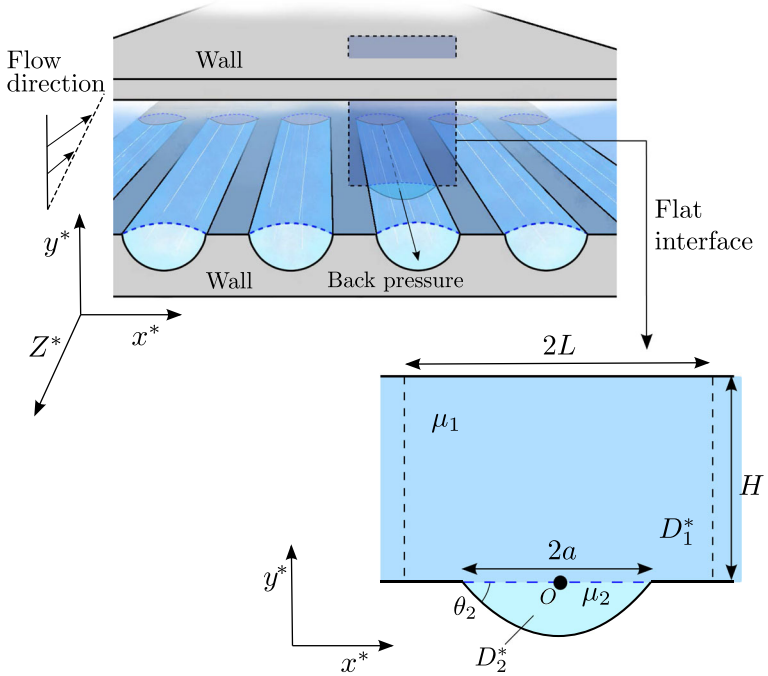

Fig. 2 Periodic channel flow involving a liquid-infused surface on the lower wall and a no-slip upper wall. The grooves are filled (or "infused") with a fluid that is generally of different viscosity to the upper working fluid. A single period window of a typical domain in the cross-plane with a flat interface $\theta_1 = 0$ is also shown

2 Problem setting

The geometry of the channel is shown in Fig. 2. Let D_1^* denote the region in a single period window containing a "working fluid" with viscosity μ_1, with D_2^* denoting the groove region containing a fluid with viscosity μ_2 and separated from fluid 1 by an interface. The lower wall of the channel outside a $2L$-periodic arrangement of grooves is at $y^* = 0$ and the upper no-slip wall of the channel above this surface is at $y^* = H$. The grooves are taken to have a circular profile protruding downwards into the surface with angle θ_2. The width of each interface in the x^* direction is $2a$, $0 < a < L$. For this study, the interfaces between the two fluids in the cross-sectional plane are taken to be flat, i.e. $\theta_1 = 0$: this is in order that the following conformal mapping formulation can be used. It should be noted, however, that in a real flow situation the interface will not remain flat for all Z^*: the present study should therefore be thought of as resolving the flow at a particular value of Z^* in a geometry that changes with Z^*. The origin of the cross-sectional (x^*, y^*) plane is at the centre of the interface in a principal period window. Steady flow of fluid 1 in the Z^*-direction along the channel is driven by an imposed constant pressure gradient. For closed grooves, this typically induces a counter, or "back", pressure gradient in the groove-based fluid 2.

Fluid 1 satisfies the two-dimensional Stokes' equations

$$\mu_1 \nabla^{*2} w_1^*(x^*, y^*) = \frac{\partial p_1^*}{\partial Z^*}, \quad (x^*, y^*) \in D_1^*, \tag{5}$$

where ∇^{*2} is a two-dimensional Laplacian $\partial_{x^*x^*} + \partial_{y^*y^*}$ with the condition $\partial w_1^*/\partial x^* = 0$ on $x^* = \pm L$ (resulting from the periodicity and symmetry) and a no-slip condition on the walls,

$$w_1^*(x^*, H) = 0, \quad -L \le x^* \le L, \tag{6}$$

$$w_1^*(x^*, 0) = 0, \quad a \le |x^*| \le L. \tag{7}$$

When the grooves are closed an induced pressure gradient implies that fluid 2 also satisfies Stokes' equations now in the form

$$\mu_2 \nabla^{*2} w_2^*(x^*, y^*) = -\mathcal{R} \frac{\partial p_1^*}{\partial Z^*}, \quad (x^*, y^*) \in D_2^*, \quad \mathcal{R} > 0. \tag{8}$$

Fluid 2 satisfies a no-slip condition on the bottom wall of the groove. Fluid 1 and 2 interact across the interface. The interfacial conditions are continuity of the velocity and of viscous stress:

$$\begin{cases} w_1^* = w_2^*, \\ \mu_1 \dfrac{\partial w_1^*}{\partial y^*} = \mu_2 \dfrac{\partial w_2^*}{\partial y^*}, \end{cases} \tag{9}$$

on $|x^*| < a$, $y^* = 0$. The net volume flux across the groove cross-section must be zero due to mass conservation at steady state:

$$\int_{D_2^*} w_2^*(x^*, y^*) \mathrm{d}x^* \mathrm{d}y^* = 0. \tag{10}$$

It is this latter condition that picks out the induced pressure gradient in the groove, i.e. it determines the parameter $\mathcal{R}$.

To non-dimensionalize the problem consider

$$(x^*, y^*) = H(x, y), \qquad w_n^* = \frac{\partial p_1^*}{\partial Z^*} \frac{H^2}{\mu_n} w_n, \quad n = 1, 2. \tag{11}$$

The governing equations (5) and (8) reduce to

$$\nabla^2 w_1 = 1, \quad (x, y) \in D_1, \tag{12}$$

and

$$\nabla^2 w_2(x, y) = -\mathcal{R}, \quad (x, y) \in D_2, \tag{13}$$

where ∇^2 denotes a two-dimensional Laplacian $\partial_{xx} + \partial_{yy}$ and the boundary conditions on the interface (9) become

$$\begin{cases} \sigma w_1 = w_2, \\ \dfrac{\partial w_1}{\partial y} = \dfrac{\partial w_2}{\partial y}, \end{cases} \tag{14}$$

on $-\delta\alpha \le x \le \delta\alpha$, $y = 0$. Now $\{D_j \mid j = 1, 2\}$ denotes the non-dimensional counterparts to $\{D_j^* \mid j = 1, 2\}$. Let C_- denote the no-slip lower circular-arc wall of the groove. The geometry is shown on the left of Fig. 3. Because of the periodicity and symmetries of the flow,

$$\frac{\partial w_1}{\partial x}(\pm\alpha, y) = 0, \quad 0 \le y \le 1. \tag{15}$$

Also, from (6) and (7), $w_1(x, y)$ and $w_2(x, y)$ satisfy the no-slip conditions:

$$w_1(x, 1) = 0, \quad -\alpha \le x \le \alpha, \tag{16}$$
$$w_1(x, 0) = 0, \quad \delta\alpha \le |x| \le \alpha, \tag{17}$$

and $w_2(x, y)$ also satisfies

$$w_2(x, y) = 0, \quad (x, y) \in C_-. \tag{18}$$

The velocities $w_1(x, y)$ and $w_2(x, y)$ can be split additively into basic Poiseuille profiles $w_{P,1}(x, y)$ and $w_{P,2}(x, y)$ and additional flows, $\hat{w}_1$ and $\hat{w}_2$, that are harmonic in regions D_1 and D_2, respectively:

$$\begin{aligned} w_1(x, y) &= w_{P,1}(x, y) + \hat{w}_1(x, y), \quad w_{P,1}(x, y) \equiv \frac{y(y-1)}{2}, \\ w_2(x, y) &= \mathcal{R} w_{P,2}(x, y) + \hat{w}_2(x, y), \end{aligned} \tag{19}$$

where

$$w_{P,2}(x, y) \equiv \frac{1}{4}\left\{ \frac{\delta^2\alpha^2}{\sin^2\theta_2} - x^2 - \left(y - \frac{\delta\alpha}{\tan\theta_2} \right)^2 \right\}. \tag{20}$$

Conditions (14) on the interface then become

$$\begin{cases} \sigma \hat{w}_1(x, 0) = \frac{\mathcal{R}}{4}\left(\delta^2\alpha^2 - x^2\right) + \hat{w}_2(x, 0), & \text{(21a)} \\ -\frac{1}{2} + \frac{\partial \hat{w}_1}{\partial y}(x, 0) = \frac{\mathcal{R}\delta\alpha}{2\tan\theta_2} + \frac{\partial \hat{w}_2}{\partial y}(x, 0), & \text{(21b)} \end{cases}$$

for $-\delta\alpha \le x \le \delta\alpha$. Neither $\hat{w}_1(x, y)$ nor $\hat{w}_2(x, y)$ are known but, since they are harmonic, they can be obtained using complex analysis techniques and conformal mapping as will now be shown.

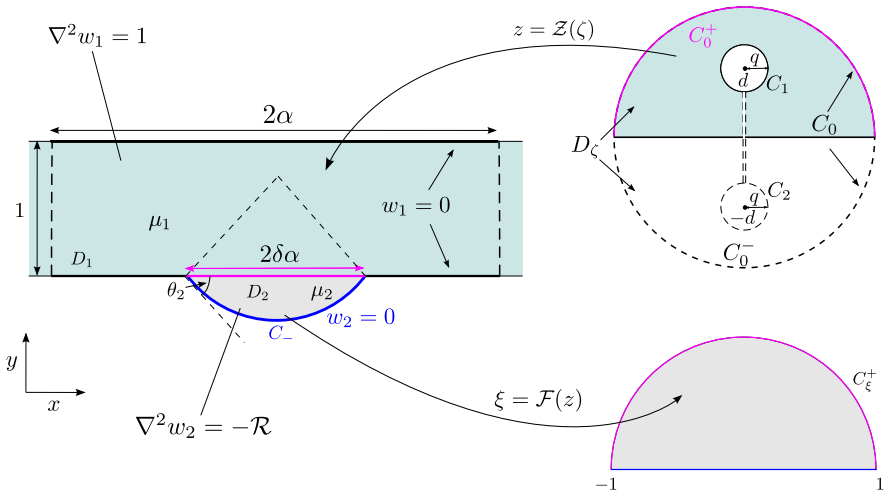

Fig. 3 Non-dimensional problem for the flow over a circular groove. The function $\mathcal{Z}(\zeta)$ is a conformal map from an upper half-disc outside of the inner circle C_1 to the period window. The function $\mathcal{F}(z)$ maps from D_2 to the upper half-disc

3 Complex analysis formulation

Consider the analytic functions (or "complex potentials") $h_1(z) \equiv \chi_1 + \mathrm{i}\hat{w}_1$ and $h_2(z) \equiv \chi_2 + \mathrm{i}\hat{w}_2$, where χ_1 and χ_2 are the harmonic conjugates of $\hat{w}_1$ and $\hat{w}_2$, respectively. Use of the Cauchy–Riemann equations changes condition (21b) to

$$-\frac{1}{2} + \frac{\partial \chi_1}{\partial x}(x, 0) = \frac{\mathcal{R}\delta\alpha}{2\tan\theta_2} + \frac{\partial \chi_2}{\partial x}(x, 0). \tag{22}$$

On integrating both sides of (22) from $-\delta\alpha$ to a general point x,

$$-\frac{1}{2}(x + \delta\alpha) + \chi_1(x, 0) = \frac{\mathcal{R}\delta\alpha}{2\tan\theta_2}(x + \delta\alpha) + \chi_2(x, 0), \tag{23}$$

where the choice $\chi_1(-\delta\alpha, 0) = \chi_2(-\delta\alpha, 0) = 0$ can be made without loss of generality. The two-fluid boundary conditions (21a) and (21b) are reduced to the following mixed interfacial conditions:

$$\begin{cases} \mathrm{Im}[h_1(z)] = \frac{\mathcal{R}}{4\sigma}\left(\delta^2\alpha^2 - (\mathrm{Re}[z])^2\right) + \frac{1}{\sigma}\mathrm{Im}[h_2(z)], & \text{(24a)} \\ \mathrm{Re}[h_1(z)] = \left(\frac{\mathcal{R}\delta\alpha}{2\tan\theta_2} + \frac{1}{2}\right)(\mathrm{Re}[z] + \delta\alpha) + \mathrm{Re}[h_2(z)]. & \text{(24b)} \end{cases}$$

The two unknown analytic functions $h_1(z)$ or $h_2(z)$ will be determined as functions of a convenient parametric variable ζ associated with a conformal mapping. Let D_ζ be a circular domain in a complex ζ-plane interior to the unit circle denoted as C_0 but exterior to two inner circles C_1 and C_2. The radii of the circles are both q and the centres are $\zeta = d$, $\zeta = -d$, where d is purely imaginary. The circular domain D_ζ is

illustrated in the upper right figure of Fig. 3. Now consider the following conformal map $\mathcal{Z}(\zeta)$ from D_ζ to the channel region D_1:

$$z = \mathcal{Z}(\zeta) = \frac{\alpha}{\pi \mathrm{i}} \log \frac{\omega(\zeta, \Theta_1(\infty))}{\omega(\zeta, \Theta_2(\infty))}, \tag{25}$$

where

$$\Theta_1(\zeta) \equiv d + \frac{q^2 \zeta}{1 - \overline{d}\zeta}, \qquad \Theta_2(\zeta) \equiv -d + \frac{q^2 \zeta}{1 + \overline{d}\zeta} = \overline{\Theta_1}(\zeta). \tag{26}$$

The overbar denotes the Schwarz conjugate of an analytic function, which is defined by $\overline{\Theta}_1(\zeta) \equiv \overline{\Theta_1(\overline{\zeta})}$. The function $\omega(\cdot, \cdot)$ is the so-called prime function that is naturally associated with the triply connected domain D_ζ. The prime function $\omega(\zeta, \gamma)$ has several important properties, the most important for present purposes is that it is analytic in D_ζ and has a simple zero when $\zeta = \gamma$: interested readers can refer to [16] for further background. The function $\mathcal{Z}(\zeta)$ maps the upper half-circle C_0^+ of the ζ-plane to the portion $\{(x, y) \mid x \in [-\delta\alpha, \delta\alpha],\ y = 0\}$, the negative real axis of the ζ-plane to the portion $\{(x, y) \mid x \in [\delta\alpha, \alpha],\ y = 0\}$, and the positive real axis of the ζ-plane to the portion $\{(x, y) \mid x \in [-\alpha, -\delta\alpha],\ y = 0\}$.

It is important to note that the same map (25) has been used to analyse flow in a periodic channel over superhydrophobic surfaces and with invaded grooves [14].

The objective now is to calculate $H_1(\zeta) \equiv h_1(\mathcal{Z}(\zeta))$ and $H_2(\zeta) \equiv h_2(\mathcal{Z}(\zeta))$. Because $\mathrm{Im}[H_1(\zeta)] = 0$ on the real axis of the ζ-plane, i.e. $\overline{\zeta} = \zeta$, then

$$\overline{H_1(\zeta)} = \overline{H_1}(\zeta) = H_1(\zeta). \tag{27}$$

By the Schwarz reflection principle, $H_1(\zeta)$ can be analytically continued to the lower half-unit disc exterior to circle C_2 defined by D_ζ^-.

The boundary condition (24a) is then reduced to

$$\mathrm{Im}[H_1(\zeta)] = \begin{cases} \dfrac{\mathcal{R}}{4\sigma}(\delta^2\alpha^2 - \mathrm{Re}[\mathcal{Z}(\zeta)]^2) + \dfrac{1}{\sigma}\mathrm{Im}[h_2(\mathcal{Z}(\zeta))] & \text{on } C_0^+, \\ -\dfrac{\mathcal{R}}{4\sigma}(\delta^2\alpha^2 - \mathrm{Re}[\mathcal{Z}(\zeta)]^2) - \dfrac{1}{\sigma}\mathrm{Im}[h_2(\mathcal{Z}(\zeta))] & \text{on } C_0^-, \\ 0 \quad \text{on } C_1,\ C_2. \end{cases} \tag{28}$$

At first sight, this resembles a classical Schwarz problem for the analytic function $H_1(\zeta)$ in the domain D_ζ. But the crucial point to note is that $h_2(z)$ is not known so the right-hand side does not constitute a given set of data for the imaginary part of $H_1(\zeta)$ on the boundary of D_ζ.

One way to proceed is to *assume* that the imaginary part of $h_2(z)$ on $C_0^\pm$ is known. Then an integral form of the solution for $H_1(\zeta)$ is given by the following Schwarz integral formula [16, 17]:

$$H_1(\zeta) = \frac{1}{2\pi}\int_{C_0} \mathrm{Im}[H_1(\zeta')][\mathrm{d}\log\omega(\zeta',\zeta) + \mathrm{d}\log\overline{\omega}(\overline{\zeta'},1/\zeta)] + c_1\mathcal{Z}(\zeta) + c_2, \tag{29}$$

where $c_1, c_2 \in \mathbb{R}$ and where the term $\mathcal{Z}(\zeta)$ has been added to account for the expected multi-valuedness of the real part of $H_1(\zeta)$ around C_1 and C_2. See [15] for more details.

Next, by using (27), condition (24b) is also reduced to the following (different) boundary value problem on D_ζ:

$$\begin{cases} \mathrm{Re}[H_1(\zeta)] = f(\zeta), & \zeta \in C_0, \\ \mathrm{Im}[H_1(\zeta)] = 0, & \zeta \in C_1,\ C_2, \end{cases} \tag{30}$$

where

$$f(\zeta) \equiv \left(\frac{\mathcal{R}\delta\alpha}{2\tan\theta_2} + \frac{1}{2}\right)(\mathrm{Re}[\mathcal{Z}(\zeta)] + \delta\alpha) + \mathrm{Re}[h_2(\mathcal{Z}(\zeta))]. \tag{31}$$

Assuming once again that the real part of $h_2(z)$ is known, this (now mixed) boundary value problem (30) can be solved uniquely by a so-called "generalized Schwarz integral" proposed recently in Miyoshi and Crowdy [15]:

$$H_1(\zeta) = \frac{1}{\eta(\zeta)}\left(I(\zeta) + \frac{\hat{C}}{\zeta-\gamma} + \mathrm{i}\hat{c}_2\right) + \hat{c}_1\mathcal{Z}(\zeta),\ \hat{c}_1, \hat{c}_2 \in \mathbb{R}, \tag{32}$$

where $\hat{C} \in \mathbb{C}$ and $I(\zeta)$ satisfies the more familiar Schwarz-type boundary value problem

$$\mathrm{Re}[I(\zeta)] = \begin{cases} \eta(\zeta)f(\zeta) - \mathrm{Re}\left[\dfrac{\hat{C}}{\zeta-\gamma}\right] & \text{on } C_0, \\ -\mathrm{Re}\left[\dfrac{\hat{C}}{\zeta-\gamma}\right] & \zeta \in C_1,\ C_2, \end{cases} \tag{33}$$

where

$$I(\zeta) \equiv \eta(\zeta)H_1(\zeta) - \frac{\hat{C}}{\zeta-\gamma}. \tag{34}$$

The parameter γ is a simple pole of the function $\eta(\zeta)$ which is a radial-slit map [16] defined by

$$\eta(\zeta) \equiv c_\eta \frac{\omega(\zeta,\beta)\omega(\zeta,1/\overline{\beta})}{\omega(\zeta,\gamma)\omega(\zeta,1/\overline{\gamma})}, \quad \beta,\gamma \in D_\zeta. \tag{35}$$

This mapping clearly also has a simple zero at β. The parameters c_η, β, and γ should be chosen so that $\eta(\zeta)$ satisfies

$$\arg[\eta(\zeta)] = \begin{cases} 0 \text{ or } \pi & \text{on } C_0, \\ \pm\dfrac{\pi}{2} & \text{on } C_1, \\ \pm\dfrac{\pi}{2} & \text{on } C_2. \end{cases} \tag{36}$$

The two integral expressions for $H_1(\zeta)$ in (29) and (32) must be consistent. This requires making the correct choice of $h_2(z)$ or, equivalently, by solving for the flow in the groove. The idea of the numerical construction is to obtain $h_2(z)$ by evaluating (29) and (32) at some collocation points $\{\zeta_m \mid m = 1, 2, \ldots, \mathcal{M}\}$ on the interface and ensuring that they are self-consistent. The technique for solving this is explained in detail in Appendix B. It makes use of another conformal mapping between a simply connected preimage region to the groove region.

After calculating the flow on the interfaces, it is possible to calculate the slip length of the channel. The (dimensional) slip length λ^* is given by the integral of $\hat{w}_1$ on the interface as follows:

$$\lambda^* = -\frac{H^2 \int_{-\delta\alpha}^{\delta\alpha} \hat{w}_1(x, 0)\, \mathrm{d}x}{L + H \int_{-\delta\alpha}^{\delta\alpha} \hat{w}_1(x, 0)\, \mathrm{d}x}. \tag{37}$$

The derivation of the slip length is explained in detail in Appendix D.

4 Testing the accuracy of the analytical formulas derived in [1]

The formulas (2) are derived in [1] under the assumption that $\delta \to 0$ and $\alpha \to 0$ and they are valid for any angles θ_1 and θ_2 shown in Fig. 1. The numerical method just described has no such restriction on δ and α but is only valid for $\theta_1 = 0$. In this special case, the general formulas (2) become simpler. Using the notation $\tilde{\lambda}^*$ to denote the slip length formula emerging from the analytical solutions in [1], and $\tilde{\mathcal{R}}$ to denote the back-pressure in the groove, it can be shown that

$$\tilde{\lambda}^* = \frac{\pi\alpha\delta^2 H}{2}\Delta = \frac{\pi a^2}{2L}\Delta, \tag{38}$$

$$\tilde{\mathcal{R}} = \frac{\mathcal{S}}{\delta\alpha(2 + \pi\alpha\delta^2\Delta)}, \tag{39}$$

where Δ and $\mathcal{S}$ are given by

$$\Delta \equiv \frac{\mathrm{i}}{\pi} \fint_{-\infty}^{\infty} k e^{-k\pi} (\rho_{b,s}(k) - \mathcal{S}\rho_{b,p}(k)) \mathrm{d}k, \tag{40}$$

and, from the formulas given in Appendix A,

$$\rho_{b,s}(k) \equiv -\frac{2\pi \mathrm{i} e^{\pi k}}{\sinh \pi k} \cdot \frac{\sinh \theta_2 k}{\mathcal{D}(k)}, \tag{41}$$

$$\rho_{b,p}(k) \equiv \frac{\pi \mathrm{i} e^{\pi k}}{\sinh \pi k} \cdot \frac{\cot \theta_2 \sinh \theta_2 k - k \cosh \theta_2 k}{\mathcal{D}(k)}, \tag{42}$$

and

$$\mathcal{S} \equiv \frac{\mathcal{Q}_1}{\mathcal{Q}_0 + \mathcal{Q}_2}, \tag{43}$$

where

$$Q_0 = \frac{1}{8}\left[\theta_2 \csc^2 \theta_2 (3 \csc^2 \theta_2 - 4) - \cot \theta_2 (3 \cot^2 \theta_2 - 4)\right], \tag{44}$$

$$Q_1 = \int_{-\infty}^{\infty} \frac{\rho_{g,s}(k)}{2\mathrm{i} \sinh \pi k} \cdot \left[e^{\theta_2 k} \frac{\sinh \theta_2 k}{\sin^2 \theta_2} - k^2 - k \cot \theta_2\right] \mathrm{d}k, \tag{45}$$

$$Q_2 = \int_{-\infty}^{\infty} \frac{\rho_{g,p}(k)}{2\mathrm{i} \sinh \pi k} \cdot \left[e^{\theta_2 k} \frac{\sinh \theta_2 k}{\sin^2 \theta_2} - k^2 - k \cot \theta_2\right] \mathrm{d}k, \tag{46}$$

with

$$\rho_{g,s}(k) = \frac{2\pi \mathrm{i} \sigma e^{-\theta_2 k}}{\mathcal{D}(k)}, \tag{47}$$

$$\rho_{g,p}(k) = \frac{\pi \mathrm{i} e^{-\theta_2 k}}{\sinh \pi k} \frac{-k \cosh \pi k + e^{k\theta_2} \cot \theta_2 \sinh \theta_2 k (\cosh \pi k + \sigma \sinh \pi k)}{\mathcal{D}(k)}, \tag{48}$$

where $\mathcal{D}(k) \equiv \sinh \theta_2 k \cosh \pi k + \sigma \sinh \pi k \cosh \theta_2 k$. The aim of this section is to test how good these formulas for $\tilde{\lambda}^*$ and $\tilde{\mathcal{R}}$ are at estimating the numerically computed values λ^* and $\mathcal{R}$.

In order to compare the results given by the analytical expressions (38) and (39) with the results of the numerical simulation, we first set $\theta_2 = \pi/2$; this corresponds to semi-circular grooves. Figure 4 shows the relative errors of $\tilde{\lambda}^*$ and $\tilde{\mathcal{R}}$ compared with the full numerical solution for a range of values of δ and α (in fact, the parameter $1/\alpha$ is used) and for several values of σ. The white regions signify that the relative error is less than 1%. As expected, the approximations (38) and (39) are found to agree well with the numerical solution when δ and α are small, with larger values of σ found to give better accuracy over a larger range. Physically, this means that the approximations work better as the viscosity contrast σ increases.

Figure 5 gives a relative error of the local velocities predicted by the analytical formulas (2) for $\theta_2 = \pi/2$ and $\sigma = 0.2$. This error is defined by

$$w_j^{*\mathrm{error}}(x^*, y^*) = \frac{|w_j^*(x^*, y^*) - \tilde{w}_j^*(x^*, y^*)|}{w_{\mathrm{av}}^*}, \qquad j = 1, 2, \tag{49}$$

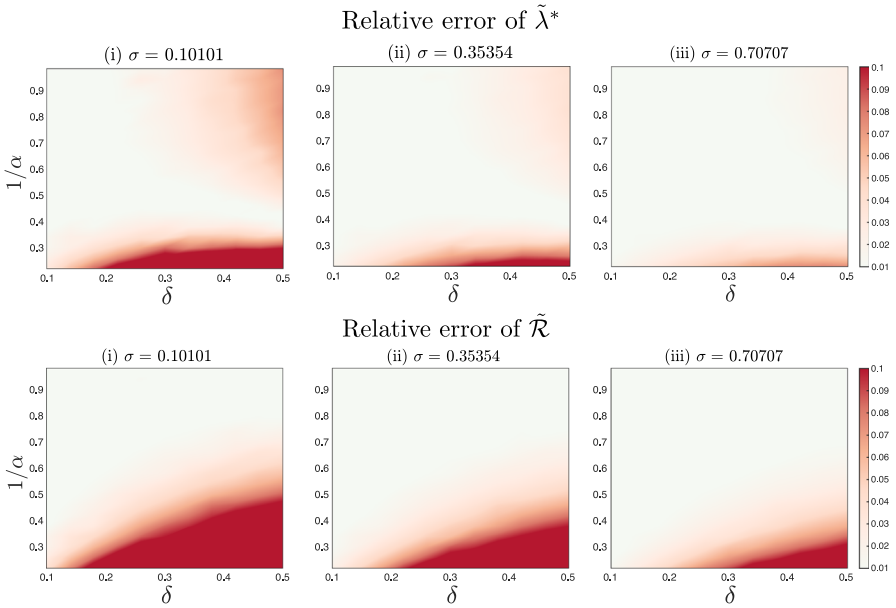

Fig. 4 Relative errors of $\tilde{\lambda}^*$ and $\tilde{\mathcal{R}}$ compared with the full numerical solution for $\theta_2 = \pi/2$ and varying values of σ plotted for a range of values of δ and $1/\alpha$. The white region shows the relative error is less than 1%. The top left-hand corner of these plots are white since this is where good agreement is expected. The red region shows the relative error is more than 10%. For σ values shown, the asymptotics work well when $\alpha \leq 2$ and $0.1 \leq \delta \leq 0.5$. The maximum relative errors of $\tilde{\lambda}^*$ and $\tilde{\mathcal{R}}$ for the case (i) are about 21% and 41%, respectively

where

$$w^*_{\text{av}} \equiv \frac{1}{\text{Area}_{D_1^*} + \text{Area}_{D_2^*}} \left[\int_{D_1^*} |w_1^*(x^*, y^*)| \mathrm{d}x^* \mathrm{d}y^* + \int_{D_2^*} |w_2^*(x^*, y^*)| \mathrm{d}x^* \mathrm{d}y^* \right]. \tag{50}$$

This choice of average velocity in the denominator is made because the local velocity can vanish. As expected, agreement is found to be excellent when α and δ are small.

Figure 6 shows a comparison of the computed normalized slip length $\lambda^*/2L$ with the result of the asymptotic formula for $\tilde{\lambda}^*/2L$ defined by (38) for different σ and δ and for $1/\alpha = 0.3$, 0.5, and 0.8. It shows that accuracy is good across all σ values but deteriorates when σ is small.

In summary, the evidence suggests that the analytical formulas (2) provide good approximants of the flows over liquid-infused surfaces in a wide range of channel geometries when $\theta_1 = 0$. While this has only been tested here for the case $\theta_1 = 0$, it is reasonable to conjecture that the formulas will continue to give good approximations for other choices of θ_1, especially if they are sufficiently small.

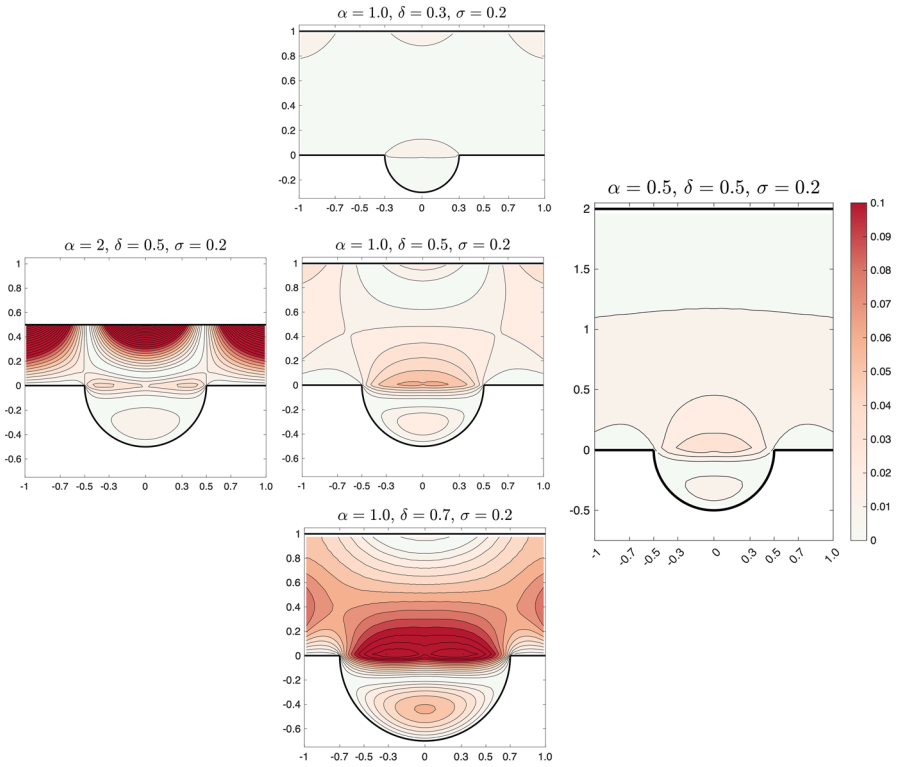

Fig. 5 Relative error in the local dimensional velocities given by the analytical predictions (2) compared with the full numerical solution for $\theta_2 = \pi/2$ and $\sigma = 0.2$ as α and δ are varied. It is confirmed that the relative error in a whole period window is less than 10% when $\alpha < 1.0$ and $\delta < 0.5$

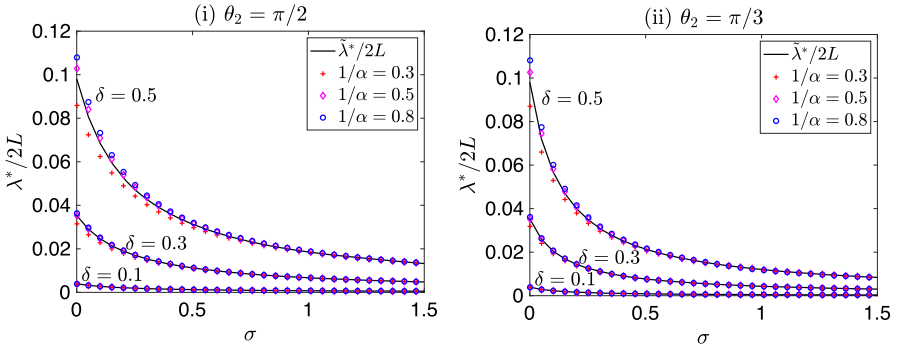

Fig. 6 Comparison of the normalized slip length $\lambda^*/2L$ with the asymptotic formula for $\tilde{\lambda}^*/2L$ defined by (38) for different viscosity contrast σ. (i) $\theta_2 = \pi/2$, and (ii) $\theta_2 = \pi/3$. Accuracy is good across all σ values but deteriorates when σ is small

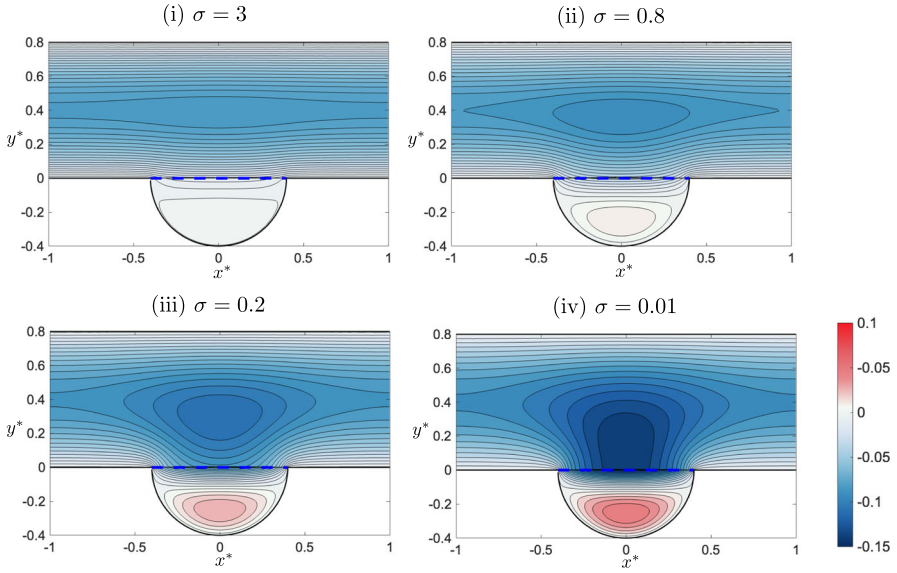

Fig. 7 Dimensional velocity contour plots of $w_1^*(x^*, y^*)$ and $w_2^*(x^*, y^*)$ with different viscosity contrasts σ. The geometrical parameters $\delta = 0.4$, $\alpha = 1.25$, and $L = 1$ are used in all figures. We have set $1/\mu_1 \cdot \partial p_1^*/\partial Z^* = 1$

5 Characterization of the solutions

Since the numerical method can be used, in principle, for any circular channel geometry with different α, δ, and σ with $\theta_1 = 0$ it is now used to compute the flows, slip lengths, and back-pressures for a range of liquid-infused surfaces. In the following calculations the choices $L = 1$ and $\dfrac{1}{\mu_1}\dfrac{\partial p_1^*}{\partial Z^*} = 1$ are made.

Figures 7 and 8 show typical velocity contour plots of $w_1^*(x^*, y^*)$ and $w_2^*(x^*, y^*)$. Figure 7 features contours for $\delta = 0.4$, $\alpha = 1.25$, $L = 1$, and $\theta_2 = \pi/2$ and several values of σ. When σ is large, the interface behaves like a "wall" because the fluid 2 is very viscous compared to fluid 1. In the upper-left panel of Fig. 7 the flow in fluid 1 is close to a Poiseuille flow in a channel; the deviation from this gets more noticeable as σ decreases. In Fig. 8 the values of δ, α, and L are fixed to be 0.5, 2, and 1 and the viscosity contrast is fixed to be $\sigma = 0.2$ while the groove shape is varied; this means several values of θ_2 are taken. The colour scheme in these figures highlights the recirculating nature of the flow in the grooves with red and blue zones travelling in opposite directions.

When $\sigma \to 0$, the two-phase condition (14) for the dimensional velocity fields w_1^* and w_2^* implies that

$$\frac{\partial w_1^*}{\partial y^*} = \sigma \frac{\partial w_2^*}{\partial y^*} \to 0 \tag{51}$$

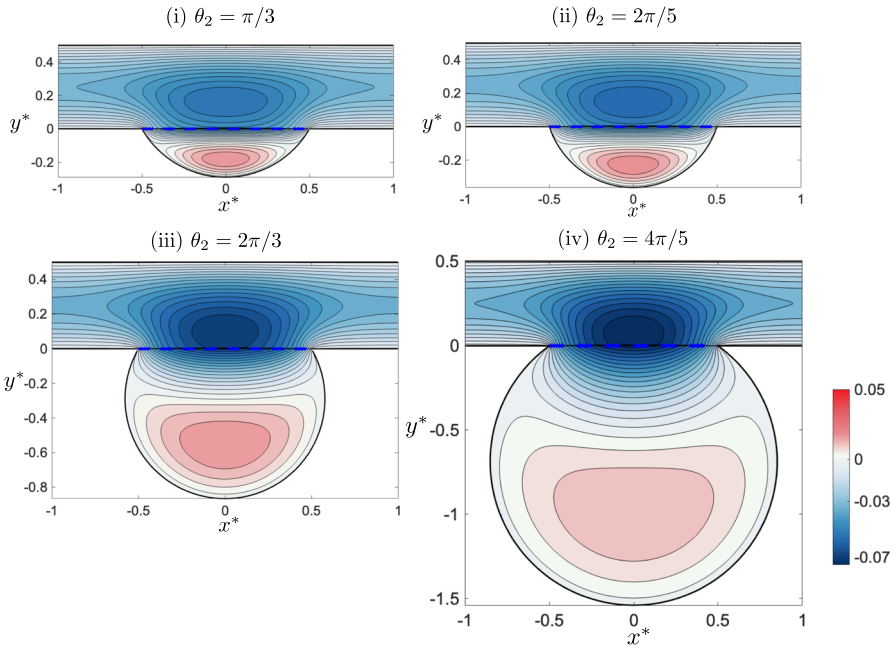

Fig. 8 Dimensional velocity contour plots of $w_1^*(x^*, y^*)$ and $w_2^*(x^*, y^*)$ for different angles θ_2 and $\sigma = 0.2$. The geometry parameters of the channel are fixed i.e. $\delta = 0.5$, $L = 1$, and $\alpha = 2$, while (i) $\theta_2 = \pi/3$, (ii) $\theta_2 = 2\pi/5$, (iii) $\theta_2 = 2\pi/3$, and (iv) $\theta_2 = 4\pi/5$. We have set $1/\mu_1 \cdot \partial p_1^*/\partial Z^* = 1$

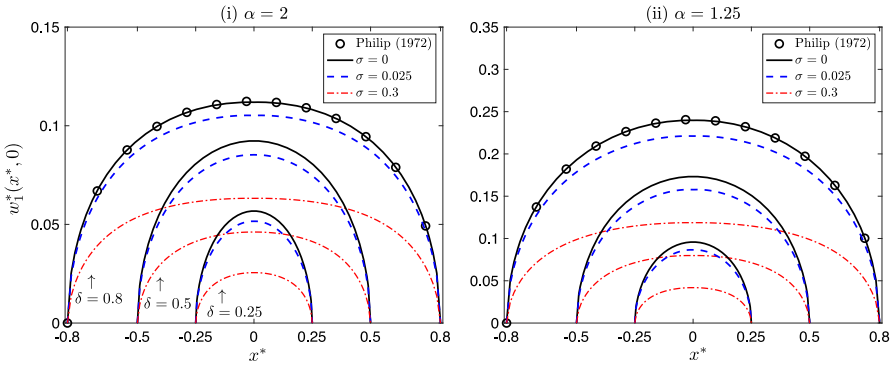

Fig. 9 The velocity profile on the interface for (i) $\alpha = 2$ and (ii) $\alpha = 1.25$ when $\delta = 0.25$, $\delta = 0.5$, and $\delta = 0.8$. We have set $L = 1$. The angle θ_2 is fixed to $\pi/2$. Note that the solution for $\sigma = 0$ corresponds to the analytical solution for the bounded channel given by Philip [18]

which corresponds to a no-shear condition on fluid 1. This situation, modelling a superhydrophobic surface, was studied by Philip [18]; Crowdy found the analogous analytical solutions for flows in annular pipes [19]. Figure 9 shows some typical interfacial velocity profiles for (i) $\alpha = 2$ and (ii) $\alpha = 1.25$ and different viscosity contrasts σ and for $\delta = 0.25$, $\delta = 0.5$, and $\delta = 0.8$. As expected the interface velocity increases as $\sigma \to 0$ since one expects a reduction in the hydrodynamic drag as σ

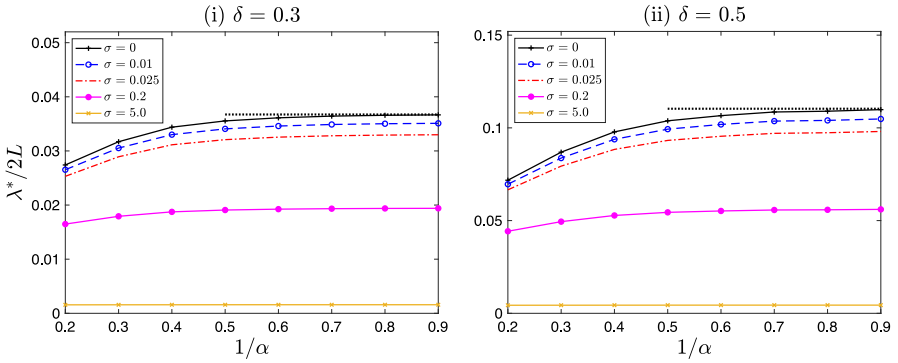

Fig. 10 Normalized slip length with respect to $1/\alpha$ for different δ. When $1/\alpha$ becomes large and $\sigma = 0$, the normalized slip length converges to Philip's result for semi-infinite shear flow over the surface (black dotted line)

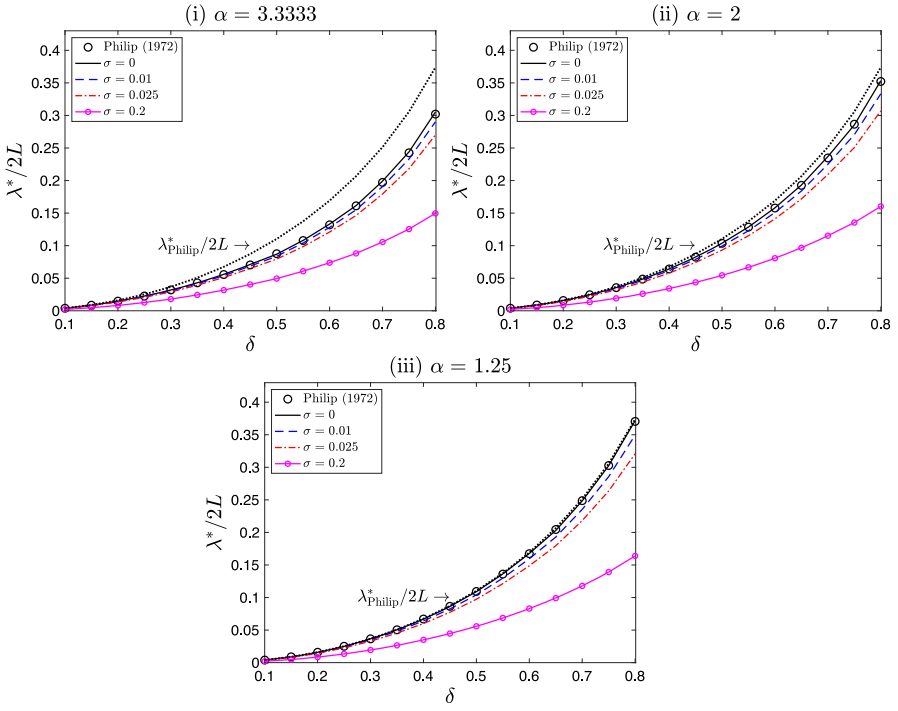

Fig. 11 Slip length with respect to δ for fixed $\theta_2 = \pi/2$ and different channel heights: (i) $\alpha = 3.3333$, (ii) $\alpha = 2$, (iii) $\alpha = 1.25$. Black circles show results from Philip's (1972) solution. When $\sigma = 0$ the calculated slip length matches Philip's slip length for the case of semi-infinite shear flow over the surface

decreases. Moreover, the velocity as $\sigma \rightarrow 0$ agrees with that calculated by Philip [18] providing a corroboration of the accuracy of the numerical scheme.

From Philip's analytical solutions [18] the corresponding slip lengths can be readily extracted. Figures 10 and 11 show the numerically computed slip length for a range of geometrical parameters, and confirms that they converge to Philip's results as $\sigma \rightarrow 0$.

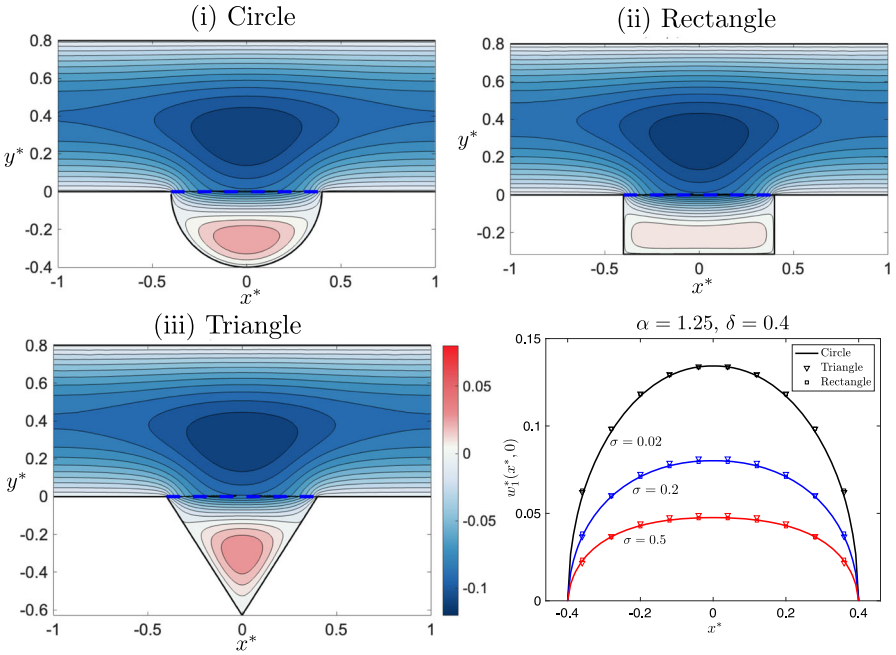

Fig. 12 (i), (ii), and (iii): Dimensional flows $w_1^*(x^*, y^*)$ and $w_2^*(x^*, y^*)$ over different groove shapes for $L = 1$, $\alpha = 1.25$, $\delta = 0.4$, $\sigma = 0.2$, and $1/\mu_1 \cdot \partial p_1^*/\partial Z^* = 1$. The areas of these grooves are chosen to be the same in each case. (Right-bottom) The interface velocities are also shown for a range of σ values. It is seen, both from the flow contours and the closely similar interface velocity profiles, that precise details of the groove shape has only weak influence on the motion of the working fluid

6 Other groove shapes

The grooves in a liquid-infused surface need not be circular. The advantage of the method presented here is that it can be easily adapted to any groove geometry (although still with $\theta_1 = 0$). This is done by simply changing the form of an aforementioned conformal mapping to the groove region. For polygonal grooves, for example, instead of $\xi = \mathcal{F}(z)$ as specified in equation (B2), conformal maps from polygonal domains to semi-circular discs can be used; these are examples of Schwarz–Christoffel mappings. For simple shapes, these mappings are easy to find analytically. For more complicated shapes, a useful numerical package for finding such maps given by [20] can be used.

Figure 12 shows the velocity contour plots of (i) a circular groove, (ii) a rectangle groove, and (iii) a triangle groove. For the polygonal-shaped regions, a basis of 30 Fourier series coefficients were used. The area of all these grooves is taken to be identical. In this case, it is observed that the velocity on the interface is similar in all cases. The results indicate the important result that the shape of the grooves does not much affect the slip length of the flow. This has practical implications for the broad applicability of the analytical formulas of [1] whose accuracy was tested earlier: it means that they can provide good flow approximants even for non-circular grooves

if one replaces the given groove geometry by an "equivalent circular groove" of the same width and area.

7 Discussion

This paper develops a new methodology for solving a two-fluid boundary value problem relevant to modelling pressure-driven channel flow over liquid-infused surfaces. This is done, following previous work by Miyoshi *et al.* [14], by considering conformal maps to the channel region from suitable triply connected circular domains. On changing the two-fluid boundary value problem to a mixed boundary value problem on those triply connected domains, the resulting problems can be solved by using "generalized Schwarz integrals" as devised recently in [15]. The slip lengths calculated here match those calculated by Philip when $\alpha \to 0$ providing a reassuring corroborative check on the formulation. As discussed in more detail in Miyoshi *et al.* [14], a significant advantage of using this preimage triply connected domain is that it "uniformizes" some of the singularities at points on the boundary where the conditions change type meaning that it naturally accounts for the singularities at such points. Other methods often require remeshing at such boundary point singularities.

A key finding is that the slip lengths and induced back-pressure found using the numerical scheme match well to those predicted by asymptotically exact analytical formulas found recently in [1], even well outside the formal range of validity of the derivation of those asymptotic formulas. This suggests those formulas provide useful theoretical tools giving good approximations to channel flows over liquid-infused surfaces over a broad range of operating conditions. This is particularly significant in view of the rarity of finding analytical descriptions of two-fluid flows. One important use of the formulas is that an ordinary differential equation approximating the evolution of $\theta_1(Z^*)$ can now be written down explicitly; such formulas help predict a phenomenon known as "shear-induced failure" of LISs [3]. Work in this direction is in progress.

Of course, the numerical method can be used with great accuracy for many flow configurations and is valuable in its own right. It has been used here to carry out a quantitative study of the slip properties of LISs in a range of configurations.

Acknowledgements The first author is grateful to The Nakajima Foundation in Japan for financial support. The second author thanks EPSRC for a studentship. This work is partly funded by EPSRC Grant EP/V062298/1.

Declarations

Conflict of interest: The authors report no conflict of interest.

Appendix A: Functions of k appearing in (4)

The functions of k appearing in formula (4) are

$$\rho_b(k) = \rho_{b,s}(k) - \mathcal{S}\rho_{b,p}(k),\ \rho_g(k) = \rho_{g,s}(k) - \mathcal{S}\rho_{g,p}(k), \tag{A1}$$

where

$$\rho_{b,s}(k) = \frac{2\pi \mathrm{i} e^{k\pi}}{\mathcal{D}(k)\sinh \pi k}\left(\sigma \cosh(\theta_1+\theta_2)k \sinh\theta_1 k - \sinh(\theta_1+\theta_2)k\cosh\theta_1 k\right), \tag{A2}$$

$$\rho_{g,s}(k) = \frac{2\pi \mathrm{i}\sigma e^{-k\theta_2}}{\mathcal{D}(k)}, \tag{A3}$$

$$\rho_{b,p}(k) = \frac{\pi \mathrm{i} e^{k\pi}}{\mathcal{D}(k)\sinh \pi k}\Bigg((\cot\theta_1+\cot\theta_2)\sinh\theta_2 k \tag{A4}$$

$$- \frac{\mathrm{cosec}^2\theta_1}{k}\sinh\theta_1 k \sinh(\theta_1+\theta_2)k\Bigg), \tag{A5}$$

$$\begin{aligned}\rho_{g,p}(k) = \frac{\pi \mathrm{i} e^{-k\theta_2}}{\mathcal{D}(k)\sinh \pi k}\Bigg(&- \cot\theta_1(\sinh\theta_1 k\cosh(\pi-\theta_1)k \\ &+ \sigma\cosh\theta_1 k\sinh(\pi-\theta_1)k) \\ &+ e^{k(\theta_1+\theta_2)}\cot\theta_2\sinh\theta_2 k(\cosh(\pi-\theta_1)k + \sigma\sinh(\pi-\theta_1)k) \\ &+ \sigma\frac{\mathrm{cosec}^2\theta_1}{k}\sinh\theta_1 k\sinh(\pi-\theta_1)k\Bigg), \\ \mathcal{S} = \frac{\mathcal{Q}_2(\theta_1,\theta_2,\sigma)}{\mathcal{Q}_0(\theta_1,\theta_2,\sigma)+\mathcal{Q}_1(\theta_1,\theta_2,\sigma)}&,\end{aligned} \tag{A6}$$

and

$$\mathcal{D}(k) = \sinh(\theta_1+\theta_2)k\cosh(\pi-\theta_1)k + \sigma\sinh(\pi-\theta_1)k\cosh(\theta_1+\theta_2)k, \tag{A7}$$

with

$$\begin{aligned}\mathcal{Q}_0(\theta_1,\theta_2,\sigma) = \frac{1}{8}\Big(&\theta_1\mathrm{cosec}^2\theta_1(3\mathrm{cosec}^2\theta_1-4) + \theta_2\mathrm{cosec}^2\theta_2(3\mathrm{cosec}^2\theta_2-4) \\ &- \cot\theta_1(3\cot^2\theta_1+1) - \cot\theta_2(3\cot^2\theta_2+1)\Big),\end{aligned} \tag{A8}$$

$$\begin{aligned}\mathcal{Q}_1(\theta_1,\theta_2,\sigma) = \fint_{-\infty}^{\infty}\frac{\rho_{g,p}(k)}{2\mathrm{i}\sinh\pi k}\Bigg(&e^{-\theta_1 k}\frac{\sinh\theta_1 k}{\sin^2\theta_1} + e^{\theta_2 k}\frac{\sinh\theta_2 k}{\sin^2\theta_2} \\ &- k(\cot\theta_1+\cot\theta_2)\Bigg)\mathrm{d}k,\end{aligned} \tag{A9}$$

$$\mathcal{Q}_2(\theta_1,\theta_2,\sigma)=\int_{-\infty}^{\infty}\frac{\rho_{g,s}(k)}{2\mathrm{i}\sinh\pi k}\left(e^{-\theta_1 k}\frac{\sinh\theta_1 k}{\sin^2\theta_1}+e^{\theta_2 k}\frac{\sinh\theta_2 k}{\sin^2\theta_2}-k(\cot\theta_1+\cot\theta_2)\right)\mathrm{d}k. \tag{A10}$$

Note that these functions depend on the two angles θ_1 and θ_2. However, they will only be tested here in the case $\theta_1 = 0$.

Appendix B: Fourier series expression for the flow on the interface

For a suitable truncation parameter N, the following expansion of $\hat{w}_2(x,0)$ on $-\delta\alpha < x < \delta\alpha$ is defined:

$$\hat{w}_2(x,0)=\sum_{n=1}^{N}a_n\cos\left(\frac{(2n-1)\pi x}{2\delta\alpha}\right),\quad a_n\in\mathbb{R}. \tag{B1}$$

The coefficients of this expansion are to be found. This is a parameterization of the imaginary part of the harmonic function $h_2(z)$ on the interface but to solve the boundary value problem (30), the real part of $h_2(z)$ is also needed. However, $h_2(z)$ has other constraints on it, in particular, its imaginary part must be zero on the semi-circular no-slip lower wall of the groove. To account for this, it is useful to introduce the following conformal map of the groove region:

$$\xi=\mathcal{F}(z)=-\frac{(\delta\alpha/z-1)^{1/2\phi}-\mathrm{i}(\delta\alpha/z+1)^{1/2\phi}}{(\delta\alpha/z-1)^{1/2\phi}+\mathrm{i}(\delta\alpha/z+1)^{1/2\phi}}, \tag{B2}$$

where $\theta_2 = \pi\phi$. This maps the groove region to the upper unit semi-circular disc in a complex ξ-plane: the interval $x\in[-\delta\alpha,\delta\alpha]$ is mapped to the upper semi-circle, and the lower boundary of the groove is mapped to the real diameter. The inverse of $\mathcal{F}(z)$ is

$$z=\mathcal{G}(\xi)=\delta\alpha\frac{[\mathrm{i}(\xi+1)]^{2\phi}-(\xi-1)^{2\phi}}{[\mathrm{i}(\xi+1)]^{2\phi}+(\xi-1)^{2\phi}}. \tag{B3}$$

Now define $H_2(\xi)\equiv h_2(\mathcal{G}(\xi))$ and define D_ξ^+ as the upper semi-disc, D_ξ^- as the lower semi-disc. Let the semi-circular boundaries of the latter regions be C_ξ^+ and C_ξ^-, respectively. Because of the no-slip boundary condition on the lower groove wall $H_2(\xi)$ satisfies $\mathrm{Im}[H_2(\xi)]=0$ on $\overline{\xi}=\xi$. By the Schwarz reflection principle,

$$H_2(\xi)=\overline{H_2(\overline{\xi})},\quad \xi\in D_\xi^-. \tag{B4}$$

Considering (B1), the boundary condition for $H_2(\xi)$ in the ξ-plane is

$$\mathrm{Im}[H_2(\xi)] \equiv \sum_{n=1}^{N} a_n r_n(\xi), \quad r_n(\xi) \equiv \begin{cases} +\cos\left(\dfrac{(2n-1)\pi \mathcal{G}(\xi)}{2\delta\alpha}\right), & \xi \in C_\xi^+, \\ -\cos\left(\dfrac{(2n-1)\pi \overline{\mathcal{G}(\bar{\xi})}}{2\delta\alpha}\right), & \xi \in C_\xi^-. \end{cases} \tag{B5}$$

This boundary value problem can be solved by the Poisson integral formula for the unit disc:

$$H_2(\xi) = a_{0,P} + \sum_{n=1}^{N} a_n P_n(\xi), \quad P_n(\xi) \equiv \frac{1}{2\pi} \oint_{C_\xi} \frac{\xi' + \xi}{\xi' - \xi} \frac{r_n(\xi')}{\xi'} \mathrm{d}\xi', \tag{B6}$$

where $C_\xi = C_\xi^+ \cup C_\xi^-$ and $a_{0,P} \in \mathbb{R}$ is a constant which can be determined by the condition $\chi_2(-\delta\alpha) = \mathrm{Re}[H_2(-1)] = 0$.

This parameterization of $h_2(z)$ allows the formulation of a linear system for the coefficients $\{a_n\}$. First, the zero-flux condition (10) of $w_2(x, y)$ is written in terms of a_n as follows:

$$\begin{aligned} \int_{D_2} w_2(x, y)\mathrm{d}x\,\mathrm{d}y &= \mathcal{R} \int_{D_2} w_{P,2}(x, y)\mathrm{d}x\,\mathrm{d}y + \sum_{n=1}^{N} a_n \int_{D_2} \mathrm{Im}[P_n(\mathcal{F}(z))]\mathrm{d}x\,\mathrm{d}y \\ &= s_0\mathcal{R} + \sum_{n=1}^{N} a_n s_n = 0, \end{aligned} \tag{B7}$$

where

$$s_0 \equiv \int_{D_2} w_{P,2}(x, y)\mathrm{d}x\,\mathrm{d}y, \quad s_n \equiv \int_{D_2} \mathrm{Im}[P_n(\mathcal{F}(z))]\mathrm{d}x\,\mathrm{d}y. \tag{B8}$$

The use of the reciprocal theorem again reduces s_n to the simple form

$$s_0 = \frac{\delta^4\alpha^4}{8\sin^2\pi\phi}\left(\frac{\pi\phi}{\sin^2\pi\phi} - \frac{1}{\tan\pi\phi}\right) - \frac{\delta^4\alpha^4}{12\tan\pi\phi}, \tag{B9}$$

and

$$s_n = \frac{1}{2}\int_{-\delta\alpha}^{\delta\alpha} x\mathrm{Re}[P_n(\mathcal{F}(z))]\mathrm{d}x + \frac{2\delta^2\alpha^2(-1)^n}{(2n-1)\pi\tan\pi\phi}, \quad n = 1, \ldots, N. \tag{B10}$$

Appendix E gives a derivation. Thus $\mathcal{R}$ can be represented in terms of the coefficients $\{a_n\}$ as

$$\mathcal{R} = -\frac{1}{s_0}\sum_{n=1}^{N} a_n s_n. \tag{B11}$$

Substituting this relation into (28) and (30), the data for each problem are now in terms of the coefficients $\{a_n\}$:

$$\mathrm{Im}[H_1(\zeta)] = \begin{cases} +\displaystyle\sum_{n=1}^{N}\frac{a_n}{\sigma}\left[-\frac{s_n}{4s_0}(\delta^2\alpha^2 - \mathrm{Re}[\mathcal{Z}(\zeta)]^2) + \mathrm{Im}[P_n(\mathcal{F}(\mathcal{Z}(\zeta)))]\right], & \zeta \in C_0^+ \\ -\displaystyle\sum_{n=1}^{N}\frac{a_n}{\sigma}\left[-\frac{s_n}{4s_0}(\delta^2\alpha^2 - \mathrm{Re}[\mathcal{Z}(\zeta)]^2) + \mathrm{Im}[P_n(\mathcal{F}(\mathcal{Z}(\zeta)))]\right], & \zeta \in C_0^- \\ 0 \quad \text{on } C_1,\ C_2, \end{cases} \tag{B12}$$

and

$$\begin{cases} \mathrm{Re}[H_1(\zeta)] = \displaystyle\sum_{n=1}^{N} a_n\left[-\frac{s_n\delta\alpha}{2s_0\tan\pi\phi}(\mathrm{Re}[\mathcal{Z}(\zeta)] + \delta\alpha) + \mathrm{Re}[P_n(\mathcal{F}(\mathcal{Z}(\zeta)))]\right] \\ \qquad\qquad + \dfrac{1}{2}(\mathrm{Re}[\mathcal{Z}(\zeta)] + \delta\alpha), \quad \zeta \in C_0, \\ \mathrm{Im}[H_1(\zeta)] = 0, \qquad \zeta \in C_1,\ C_2. \end{cases} \tag{B13}$$

In order to derive the linear system for the coefficients $\{a_n\}$, it is convenient to define functions which satisfy the following boundary conditions:

$$\mathrm{Im}[V_n(\zeta)] = \begin{cases} -\dfrac{s_n}{4s_0\sigma}(\delta^2\alpha^2 - \mathrm{Re}[\mathcal{Z}(\zeta)]^2) + \dfrac{1}{\sigma}\mathrm{Im}[P_n(\mathcal{F}(\mathcal{Z}(\zeta)))], & \zeta \in C_0^+, \\ +\dfrac{s_n}{4s_0\sigma}(\delta^2\alpha^2 - \mathrm{Re}[\mathcal{Z}(\zeta)]^2) - \dfrac{1}{\sigma}\mathrm{Im}[P_n(\mathcal{F}(\mathcal{Z}(\zeta)))], & \zeta \in C_0^-, \\ 0 \quad \text{on } C_1,\ C_2, \end{cases} \tag{B14}$$

$$\begin{cases} \mathrm{Re}[T_n(\zeta)] = -\dfrac{s_n\delta\alpha}{2s_0\tan\pi\phi}(\mathrm{Re}[\mathcal{Z}(\zeta)] + \delta\alpha) + \mathrm{Re}[P_n(\mathcal{F}(\mathcal{Z}(\zeta)))], & \zeta \in C_0, \\ \mathrm{Im}[T_n(\zeta)] = 0, \qquad \zeta \in C_1,\ C_2, \end{cases} \tag{B15}$$

and

$$\begin{cases} \mathrm{Re}[R(\zeta)] = \dfrac{1}{2}(\mathrm{Re}[\mathcal{Z}(\zeta)] + \delta\alpha), & \zeta \in C_0, \\ \mathrm{Im}[R(\zeta)] = 0, \qquad \zeta \in C_1,\ C_2. \end{cases} \tag{B16}$$

An over-determined linear system for the coefficients $\underline{\boldsymbol{a}} = (a_1, a_2, \cdots, a_N)^\top$ now follows as

$$M_1 \underline{\boldsymbol{a}} = M_2 \underline{\boldsymbol{a}} + \underline{\boldsymbol{r}}, \tag{B17}$$

where

$$M_1 = \begin{pmatrix} V_1(\zeta_1) & V_2(\zeta_1) & \cdots & V_N(\zeta_1) \\ V_1(\zeta_2) & V_2(\zeta_2) & \ddots & V_N(\zeta_2) \\ \vdots & \ddots & \ddots & \vdots \\ V_1(\zeta_{\mathcal{M}}) & V_2(\zeta_{\mathcal{M}}) & \cdots & V_N(\zeta_{\mathcal{M}}) \end{pmatrix}, \tag{B18}$$

and

$$M_2 = \begin{pmatrix} T_1(\zeta_1) & T_2(\zeta_1) & \cdots & T_N(\zeta_1) \\ T_1(\zeta_2) & T_2(\zeta_2) & \ddots & T_N(\zeta_2) \\ \vdots & \ddots & \ddots & \vdots \\ T_1(\zeta_{\mathcal{M}}) & T_2(\zeta_{\mathcal{M}}) & \cdots & T_N(\zeta_{\mathcal{M}}) \end{pmatrix}, \tag{B19}$$

and $\underline{\boldsymbol{r}} \equiv (R(\zeta_1), R(\zeta_2), \cdots, R(\zeta_{\mathcal{M}}))^\top$ and where the collocation points are defined as $\{\zeta_m \mid m = 1, \ldots, \mathcal{M}\}$ where $\mathcal{M} > N$. This system can be solved by the method of least-squares.

Once the components of these matrices are calculated, they can be used to calculate for the flow for a different viscosity contrast σ in the same geometry. When the viscosity contrast σ is changed to $\hat{\sigma}$, say, the matrices satisfy the linear transformations:

$$M_1 \to \frac{\sigma}{\hat{\sigma}} M_1, \quad M_2 \to M_2, \quad \underline{\boldsymbol{r}} \to \underline{\boldsymbol{r}}. \tag{B20}$$

This reduces computational time since it is not necessary to reconstruct new matrices when σ is changed.

Appendix C: Numerical calculation of the flow

Analytical formulas have been derived for the solution in terms of the prime function $\omega(.,.)$ associated with the triply connected domain D_ζ. To calculate the flow, plot the velocity contours, and calculate effective slip lengths it is clearly necessary to be able to evaluate the prime function $\omega(.,.)$ and there are (at least) two ways to do this.

The most numerically efficient method is to make use of freely available MATLAB codes that compute $\omega(.,.)$ for any user-specified circular domain akin to D_ζ [16, 21]. These codes are based on a numerical algorithm described in detail in [22] and which extends an earlier algorithm proposed by Crowdy and Marshall [23].

For a triply connected domain, however, it is also known (see Chap. 14 of [16]) that the infinite product representation

$$\omega(z,\zeta) = (z-\zeta)\prod_{\Theta\in\Theta''}\frac{(\Theta(z)-\zeta)(\Theta(\zeta)-z)}{(\Theta(z)-z)(\Theta(\zeta)-\zeta)}, \tag{C1}$$

is convergent; here each function Θ lies in the set of Möbius maps Θ'' which denotes all elements of the free Schottky group generated by the basic Möbius maps $\{\Theta_j, \Theta_j^{-1} : j = 1, 2\}$ except for the identity and excluding all inverses [16, 22, 23]. For numerical purposes of evaluation it is necessary to truncate this product, and the natural way to do so is to include all Möbius maps up to a chosen *level*: see [16, 23] for more details. Use of this infinite product is feasible for most channel geometries, but maintaining a required degree of accuracy requires truncation at increasingly high levels as the radii of C_1 and C_2 get larger; then convergence of the product can become unacceptably slow. In such cases, use of the MATLAB code from [21] is preferred and advised.

The parameters d and q are determined uniquely, for a given channel geometry, by solving the two equations

$$\mathcal{Z}(-1) = \delta\alpha, \qquad \mathcal{Z}(d+q\mathrm{i}) = \mathrm{i} \tag{C2}$$

subject to the constraints $|d|+q<1$, $|d|>0$, and $q>0$. Equations (C2) are readily solved using any nonlinear solver such as Newton's method.

Equally spaced collocation points on the interface are chosen in all numerical calculations. To be more precise, the collocation points $\zeta_m \in C_0$ are chosen so that

$$\mathcal{Z}(\zeta_m) = \delta\alpha\left(-1+\frac{m-1}{M-1}\right), \qquad m=1,\ldots,M. \tag{C3}$$

The coordinates of ζ_m are obtained easily by the standard interpolation methods. Both the number of coefficients a_n and the collocation points are set to be 100.

When δ is greater than 0.5, the inner circles C_1 and C_2 approach the unit circle. In this case, the appropriate radial-slit map is difficult to find, and even if it is found, the condition number of the radial-slit map defined by

$$\mathrm{cond} \equiv \max_{m=0,1,2}\left(\max_{\zeta_1,\zeta_2\in C_m}\left|\frac{\eta(\zeta_1)}{\eta(\zeta_2)}\right|\right) \tag{C4}$$

increases. In that case it is recommended that $\eta(\zeta)$ should be replaced by a *product* of radial-slit maps defined by

$$\eta(\zeta) = \hat{c}_\eta\prod_{k=1}^{K}\frac{\omega(\zeta,\beta_k)\omega(\zeta,1/\overline{\beta_k})}{\omega(\zeta,\gamma_k)\omega(\zeta,1/\overline{\gamma_k})}, \quad K>1, \tag{C5}$$

Table 1 Dimensional velocity $w_1^*(x^*, 0)$ and $\tilde{w}_1^*(x^*, 0)$ on the interface when $\delta = 0.05, \alpha = 1$, and $L = 1$ when $\sigma = 0.3$. Both the number of coefficients for the Fourier expansions of $\hat{w}_2(x, 0)$ and the collocation points are set to be 100. For the calculation of the Schwarz integral, 1500 equally spaced points are used

	$w_1^*(x^*, 0)$	$\tilde{w}_1^*(x^*, 0)$	Relative error
$x^* = 0$	−0.010665909	−0.010665102	7.6×10^{-5}
$x^* = 0.025$	−0.009489365	−0.009489434	7.2×10^{-6}
$x^* = 0.05$	−0.000000000	−0.000000000	–

Table 2 Dimensional velocity $w_1^*(x^*, 0)$ on the interface when $\delta = 0.8, \alpha = 1.25$, and $L = 1$ when $\sigma = 0$. The results are compared against Philip's solution for a bounded channel [18]. Both the number of coefficients for the Fourier expansions of $\hat{w}_2(x, 0)$ and the collocation points are set to be 100. For the calculation of the Schwarz integral, 1500 equally spaced points are used

	$w_1^*(x^*, 0)$	Philip [18]	Relative error
$x^* = 0.2$	−0.23398924	−0.23397521	5.99×10^{-5}
$x^* = 0.3$	−0.22516067	−0.22516347	1.24×10^{-5}

since the additional degrees of freedom lead to a reduction in the condition number and a more robust algorithm.

When the protrusion angle $\theta_2 \geq \pi/2$, it is recommended to use a Laurent series expansion in ξ of the Poisson integral (B6) to reduce computation time. When $\theta_2 < \pi/2$, it was observed that the number of coefficients in this Laurent series needed to retain accuracy becomes large and, in that case, the original Poisson integral (B6) is preferable.

To validate the accuracy of our numerical computation, the dimensional velocity $w_1^*(x^*, 0)$ on the interface is compared with the velocity calculated by the asymptotics $\tilde{w}_1^*(x^*, 0)$. Table 1 shows these values for $x^* = 0,\ 0.025$, and 0.05, and the relative errors when $\delta = 0.05, \alpha = 1$, and $\sigma = 0.3$. In this geometry, it is natural to consider that the flow in the period window should be approximated well by the asymptotics. Table 1 suggests that our numerical computation might be accurate for 7 digits when 100 Fourier coefficients are used. For the calculation of the Schwarz integral, 1500 equally spaced points are used.

We have also compared the flow for $\sigma = 0$ against Philip's solution for a bounded channel [18] when $\delta = 0.8, \alpha = 1.25$, and $L = 1$. Table 2 shows the dimensional velocity when $x^* = 0.2$ and 0.3, and the relative errors. Our numerical scheme also produces approximately 5.0×10^{-5} errors when 100 Fourier coefficients are used.

Appendix D: Calculation of the slip lengths

Once $w_1(x, y)$ has been determined, the effective slip lengths associated with the flow can be calculated. To do so, the approach proposed by Crowdy [7] is adapted where reciprocity arguments are used to determine the volume flux in the period window.

The total flux Q_F in the original period window D_1^* is given by

$$Q_F \equiv \int_{D_1^*} w_1^*(x^*, y^*)\mathrm{d}x^*\mathrm{d}y^* = \frac{\partial p_1^*}{\partial Z^*}\frac{H^4}{\mu_1}\int_{D_1} w_1(x, y)\mathrm{d}x\mathrm{d}y$$
$$= \frac{\partial p_1^*}{\partial Z^*}\frac{H^4}{\mu_1}\int_{D_1}(w_{P,1}+\hat{w}_1)\mathrm{d}x\mathrm{d}y = \frac{\partial p_1^*}{\partial Z^*}\frac{1}{\mu_1}\left(-\frac{1}{6}H^3L + H^4\int_{D_1}\hat{w}_1\mathrm{d}x\mathrm{d}y\right), \tag{D1}$$

the second term is evaluated using Green's second identity. By reciprocity,

$$\int_{D_1}(w_{P,1}\nabla^2\hat{w}_1 - \hat{w}_1\nabla^2 w_{P,1})\mathrm{d}x\mathrm{d}y = \oint_{\partial D_1}\left(w_{P,1}\frac{\partial\hat{w}_1}{\partial \boldsymbol{n}} - \hat{w}_1\frac{\partial w_{P,1}}{\partial \boldsymbol{n}}\right)\mathrm{d}s, \tag{D2}$$

where $\boldsymbol{n}$ is the normal vector pointing out the channel region and s is an element of arc lengths of the boundary of D_1. The symmetry at $x = \pm\alpha$ and the properties of $w_{P,1}(x, y)$ reduce this relation to

$$-\int_{D_1}\hat{w}_1\mathrm{d}x\mathrm{d}y = -\frac{1}{2}\int_{-\delta\alpha}^{\delta\alpha}\hat{w}_1(x, 0)\mathrm{d}x, \tag{D3}$$

and thus,

$$Q_F = \frac{\partial p_1^*}{\partial Z^*}\frac{1}{\mu_1}\left(-\frac{1}{6}H^3L + \frac{H^4}{2}\int_{-\delta\alpha}^{\delta\alpha}\hat{w}_1(x, 0)\mathrm{d}x\right). \tag{D4}$$

This flux is to be compared with that associated with a "comparison flow": that of the channel flow with a Navier-slip condition with Navier-slip parameter λ^* on a flat boundary taken at the level of the interface. The comparison flow field $w_\lambda^*(x^*, y^*)$ satisfies

$$\mu_1\nabla^{*2}w_\lambda^*(x^*, y^*) = \frac{\partial p_1^*}{\partial Z^*}, \qquad (x^*, y^*) \in D_1^*, \tag{D5}$$
$$w_\lambda^* = \lambda^*\frac{\partial w_\lambda^*}{\partial \boldsymbol{n}}, \qquad -L \le x^* \le L, \quad y^* = 0, \tag{D6}$$
$$w_\lambda^* = 0, \qquad -L \le x^* \le L, \quad y^* = H, \tag{D7}$$
$$\frac{\partial w_\lambda^*}{\partial x^*} = 0, \qquad x^* = \pm L, \tag{D8}$$

where $\boldsymbol{n}$ denotes the normal pointing into the liquid in this case. Here λ is the effective slip length of the channel. This problem is solved explicitly by

$$w_\lambda^* = \frac{\partial p_1^*}{\partial Z^*}\frac{1}{\mu_1}\left[\frac{y^*(y^*-H)}{2} + \frac{\lambda^*H}{2(\lambda^*+H)}(y^*-H)\right]. \tag{D9}$$

The total flux produced by w_λ^* is then calculated as follows:

$$Q_\lambda = \int_{D^*} w_\lambda^*(x^*, y^*)\mathrm{d}x^*\mathrm{d}y^* = \frac{\partial p_1^*}{\partial Z^*}\frac{1}{\mu_1}\left(-\frac{1}{6}H^3L - \frac{\lambda^* H^3 L}{2(\lambda^* + H)}\right). \tag{D10}$$

By equating Q_F to Q_λ, the effective slip length can be written in terms of the integral of $\hat{w}_1(x, 0)$ on the interface as follows:

$$\lambda^* = -\frac{H^2\int_{-\delta\alpha}^{\delta\alpha}\hat{w}_1(x, 0)\mathrm{d}x}{L + H\int_{-\delta\alpha}^{\delta\alpha}\hat{w}_1(x, 0)\mathrm{d}x}. \tag{D11}$$

Appendix E: Reciprocity

This appendix explains how to derive (B9) and (B10). By Gauss's divergence theorem,

$$\int_{D_2}(w_{P,2}\nabla^2 w_{P,2} + \nabla w_{P,2}\cdot\nabla w_{P,2})\mathrm{d}x\,\mathrm{d}y = \int_{\partial D_2} w_{P,2}\frac{\partial w_{P,2}}{\partial \boldsymbol{n}}\mathrm{d}s. \tag{E1}$$

The right-hand side becomes

$$\int_{\partial D_2} w_{P,2}\frac{\partial w_{P,2}}{\partial \boldsymbol{n}}\mathrm{d}s = \frac{\delta\alpha}{2\tan\pi\phi}\int_{-\delta\alpha}^{\delta\alpha}\frac{1}{4}(\delta^2\alpha^2 - x^2)\mathrm{d}x = \frac{\delta^4\alpha^4}{6\tan\pi\phi}. \tag{E2}$$

By direct calculation, it can be shown that

$$\int_{D_2}\nabla w_{P,2}\cdot\nabla w_{P,2}\mathrm{d}x\,\mathrm{d}y = \frac{1}{4}\int_{D_2}\left\{x^2 + \left(y - \frac{\delta\alpha}{\tan\pi\phi}\right)^2\right\}\mathrm{d}x\,\mathrm{d}y \tag{E3}$$

$$= \frac{\delta^2\alpha^2}{4\sin^2\pi\phi}\int_{D_2}\mathrm{d}x\,\mathrm{d}y - \int_{D_2} w_{P,2}\mathrm{d}x\,\mathrm{d}y \tag{E4}$$

$$= \frac{\delta^4\alpha^4}{4\sin^2\pi\phi}\left(\frac{\pi\phi}{\sin^2\pi\phi} - \frac{1}{\tan\pi\phi}\right) - \int_{D_2} w_{P,2}\mathrm{d}x\,\mathrm{d}y. \tag{E5}$$

Since $\nabla^2 w_{P,2} = -1$, Eq. (E1) becomes

$$-\int_{D_2} w_{P,2}\mathrm{d}x\,\mathrm{d}y + \frac{\delta^4\alpha^4}{4\sin^2\pi\phi}\left(\frac{\pi\phi}{\sin^2\pi\phi} - \frac{1}{\tan\pi\phi}\right) - \int_{D_2} w_{P,2}\mathrm{d}x\,\mathrm{d}y = \frac{\delta^4\alpha^4}{6\tan\pi\phi}.$$

Expression (B9) then follows.

For s_n, it is convenient to define $P_n(\mathcal{F}(z)) \equiv f_n(x, y) + \mathrm{i}g_n(x, y)$. Consider

$$\int_{D_2} g_n(x, y)\mathrm{d}x\,\mathrm{d}y = \int_{D_2}(w_{P,2}\nabla^2 g_n - g_n\nabla^2 w_{P,2})\mathrm{d}x\,\mathrm{d}y$$

$$
\begin{aligned}
&= \int_{\partial D_2} \left(w_{P,2} \frac{\partial g_n}{\partial \boldsymbol{n}} - g_n \frac{\partial w_{P,2}}{\partial \boldsymbol{n}} \right) \mathrm{d}s \\
&= \frac{1}{4} \int_{-\delta\alpha}^{\delta\alpha} (\delta^2\alpha^2 - x^2) \frac{\partial f_n}{\partial x}(x,0)\mathrm{d}x - \frac{\delta\alpha}{2\tan\pi\phi} \int_{-\delta\alpha}^{\delta\alpha} g_n(x,0)\mathrm{d}x \\
&= \frac{1}{2} \int_{-\delta\alpha}^{\delta\alpha} x f_n(x,0)\mathrm{d}x - \frac{\delta\alpha}{2\tan\pi\phi} \int_{-\delta\alpha}^{\delta\alpha} g_n(x,0)\mathrm{d}x, \qquad \text{(E6)}
\end{aligned}
$$

where the Cauchy–Riemann equations have been used in the third equality. Because $g_n(x,0) = \mathrm{Im}[P_n(\mathcal{F}(z))] = \cos((2n-1)\pi x/2\delta\alpha)$, the second term of (E6) can be calculated leading to the equation for s_n.

References

1. Rodriguez-Broadbent H, Miyoshi H, Crowdy DG. Asymptotically exact formulas for channel flows over liquid-infused surfaces. IMA J. Appl. Math. (submitted)
2. Hardt S, McHale G (2022) Flow and drop transport along liquid-infused surfaces. Ann Rev Fluid Mech 54:83–104
3. Wexler JS, Jacobi I, Stone HA (2015) Shear-driven failure of liquid infused surfaces. Phys Rev Lett 114:168301
4. Schönecker C, Hardt S (2013) Longitudinal and transverse flow over a cavity containing a second immiscible fluid. J Fluid Mech 717:376–394
5. Schönecker C, Baier T, Hardt S (2014) Influence of the enclosed fluid on the flow over a microstructured surface in the Cassie state. J Fluid Mech 740:168–195
6. Nizkaya TV, Asmolov ES, Vinogradova OI (2014) Gas cushion model and hydrodynamic boundary conditions for superhydrophobic textures. Phys Rev E 90:043017
7. Crowdy DG (2017) Perturbation analysis of subphase gas and meniscus curvature effects for longitudinal flows over superhydrophobic surfaces. J Fluid Mech 822:307–326
8. Ng C-O, Chu HC, Wang C (2010) On the effects of liquid-gas interfacial shear on slip flow through a parallel-plate channel with superhydrophobic grooved walls. Phys Fluids 22(10):102002
9. Ge Z, Holmgren H, Kronbichler M, Brandt L, Kreiss G (2018) Effective slip over partially filled microcavities and its possible failure. Phys Rev Fluids 3(5):054201
10. Liu Y, Wexler JS, Schönecker C, Stone HA (2016) Effect of viscosity ratio on the shear-driven failure of liquid-infused surfaces. Phys Rev Fluids 1:074003
11. Game S, Hodes M, Keaveny E, Papageorgiou D (2017) Physical mechanisms relevant to flow resistance in textured microchannels. Phys Rev Fluids 2(9):094102
12. Game S, Hodes M, Papageorgiou D (2019) Effects of slowly-varying meniscus curvature on internal flows in the Cassie state. J Fluid Mech 872:272–307
13. Ji S, Li H, Du Z, Lv P, Duan H (2023) Influence of interfacial coupled flow on slip boundary over a microstructured surface. Phys Rev Fluids 8(5):054003
14. Miyoshi H, Rodriguez-Broadbent H, Curran A, Crowdy DG (2022) Longitudinal flow in superhydrophobic channels with partially invaded grooves. J Eng Math 137(1):1–17
15. Miyoshi H, Crowdy DG (2023) Generalized schwarz integral formulae for multiply connected domains. SIAM Appl Math 83(3):966–984
16. Crowdy DG (2020) Solving problems in multiply connected domains. SIAM, Philadelphia
17. Crowdy DG (2008) The Schwarz problem in multiply connected domains and the Schottky-Klein prime function. Complex Var Elliptic Equ 53(3):221–236
18. Philip JR (1972) Flows satisfying mixed no-slip and no-shear conditions. Zeitschrift für angewandte Mathematik und Physik ZAMP 23(3):353–372
19. Crowdy DG (2021) Superhydrophobic annular pipes: a theoretical study. J Fluid Mech 906:15
20. Driscoll TA (1996) Algorithm 756: a matlab toolbox for Schwarz-Christoffel mapping. ACM Trans Math Softw (TOMS) 22(2):168–186
21. Github website. https://github.com/ACCA-Imperial (ACCA)

22. Crowdy DG, Kropf EH, Green CC, Nasser MMS (2016) The Schottky-Klein prime function: a theoretical and computational tool for applications. IMA J Appl Math 81(3):589–628
23. Crowdy DG, Marshall JS (2007) Computing the Schottky-Klein prime function on the Schottky double of planar domains. Comput Methods Funct Theory 7:293–308